

ChemComm

Accepted Manuscript



This is an *Accepted Manuscript*, which has been through the Royal Society of Chemistry peer review process and has been accepted for publication.

Accepted Manuscripts are published online shortly after acceptance, before technical editing, formatting and proof reading. Using this free service, authors can make their results available to the community, in citable form, before we publish the edited article. We will replace this *Accepted Manuscript* with the edited and formatted *Advance Article* as soon as it is available.

You can find more information about *Accepted Manuscripts* in the [Information for Authors](#).

Please note that technical editing may introduce minor changes to the text and/or graphics, which may alter content. The journal's standard [Terms & Conditions](#) and the [Ethical guidelines](#) still apply. In no event shall the Royal Society of Chemistry be held responsible for any errors or omissions in this *Accepted Manuscript* or any consequences arising from the use of any information it contains.

COMMUNICATION

Creating High Quality Ca:TiO₂-B (CaTi₅O₁₁) and TiO₂-B Epitaxial Thin Films by Pulsed Laser Deposition †

Cite this: DOI: 10.1039/x0xx00000x

Received 00th January 2015,
Accepted 00th January 2015Kui Zhang,^a Xianfeng Du,^a Michael B. Katz,^a Baihai Li,^a Sung Joo Kim,^a Kaixin Song,^a George W. Graham^a and Xiaoqing Pan^{*b}

DOI: 10.1039/x0xx00000x

www.rsc.org/

We demonstrate, in great detail, a completely waterless synthesis route to produce highly crystalline epitaxial thin films of TiO₂-B and its more stable variant CaTi₅O₁₁, using pulsed laser deposition (PLD).

The bronze polymorph of titanium dioxide (TiO₂-B) is interesting for many applications including high rate energy storage, solar cells, photocatalysis, thermoelectrics and sensing, owing to its uniquely layered structure and highly asymmetric unit cell. However, such a metastable phase is extremely hard to obtain with high purity and crystallinity, significantly impeding its development in these fields. After more than 30 years since the first synthesis of TiO₂-B in 1980,¹ hydrothermal methods are still the dominant route to produce this material.²⁻¹² The purity is often limited by unreacted precursors and the unavoidable presence of structural water,^{13,14} largely due to the fact that TiO₂-B is less stable than other polymorphs such as anatase and rutile,¹⁵ which leads to the lack of good baseline property tests and the absence of a true 'bulk' to distinguish between bulk effects and surface effects. Therefore, a new method to synthesize high quality TiO₂-B crystal is highly desired.

Using first principles calculations, x-ray diffraction (XRD) and atomic resolution scanning transmission electron microscopy (STEM), we have identified a stable derivative of the TiO₂-B structure, CaTi₅O₁₁ (referred to as Ca:TiO₂-B below), and have demonstrated that it can be used as an anode material in lithium-ion batteries with significantly enhanced rate capability via orientation engineering.¹⁶ In this paper, we report a synthesis approach to create high quality films of the Ca:TiO₂-B phase which can be used as a template for the waterless synthesis of pure TiO₂-B. We will discuss the optimization of the PLD growth conditions, including target composition, choice of substrates, growth temperature, laser energy and O₂ partial pressure, to achieve the best purity and crystallinity for the Ca:TiO₂-B and TiO₂-B phases. The growth mechanism and

various microstructures in the thin films are clearly shown at the atomic scale. Our findings can serve as guidelines for creating these materials in a controlled form, providing well-defined lattice orientation and surfaces for future research efforts.

According to our theoretical calculations, the Ca:TiO₂-B phase in a Ca₄Ti₂₀O₄₄ unit cell is a thermodynamically stable member of the CaO-TiO₂ pseudo-binary system, and its lattice constants are shown in Table S1 (ESI†). The PLD targets were constructed by mixing anatase TiO₂ and CaO powders, which were then sintered and pressed into dense pellets. Although the CaTi₅O₁₁ stoichiometry corresponds to a Ti:Ca ratio of 5:1, or equivalently, 1/6 (by mole) CaO in the mixture, we made targets containing 10%, 16.7% and 20% CaO for comparison. The targets were installed in a PLD chamber with a base pressure <10⁻⁷ Torr, facing substrates at a distance of 6.25 cm. A 248 nm KrF excimer laser with a pulse duration of 22 ns was used for ablating the targets at a 10 Hz repetition rate.

SrTiO₃ substrates are intrinsically fitting for growing TiO₂ based structures on top, as a previous study illustrated that SrTiO₃ (001) has a TiO₂-rich surface.¹⁷ Further, good epitaxy of (001) Ca:TiO₂-B thin films on (001) SrTiO₃ substrates is expected because its in-plane *a* and *b* cell parameters are nearly integer multiples of the lattice constant of cubic SrTiO₃ (3.905 Å), presenting a lattice mismatch of ~3.25% (calculated for diagonal mismatch). Figure 1a compares the θ -2 θ patterns of the thin films deposited from the targets of different compositions onto (001) SrTiO₃ substrates at 800 °C in an oxygen ambient of 0.05 Torr, where the laser pulse energy was set to 200 mJ (a fluence of ~3.4 J cm⁻²). With 10% CaO in the target, multiple 0_h peaks of Ca:TiO₂-B are seen at 2 θ angles corresponding to the theoretical calculations. The insufficiency of Ca caused some grains to crystallize in the anatase phase, the (001) plane of which also has a small lattice mismatch (-3.15%) with SrTiO₃ (001), evidenced by a prominent anatase 004 peak in XRD. Figure 1c shows a high angle annular dark field (HAADF) STEM image taken along the [010]

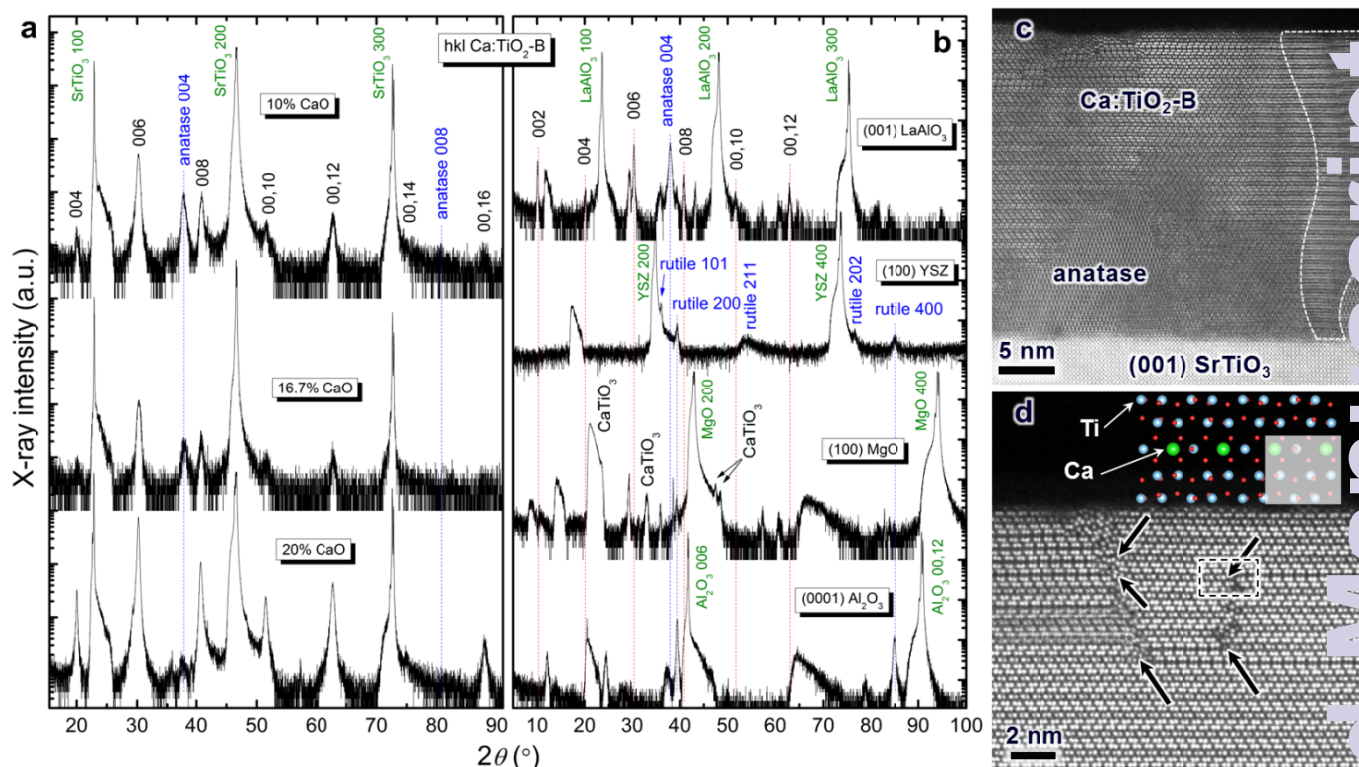


Figure 1. a) XRD patterns of thin films deposited from targets of different compositions. The 20% CaO (80% TiO₂, by mole) target resulted in a (001) Ca:TiO₂-B film with highest crystalline quality and only a trace amount of anatase. b) XRD patterns of the films deposited from a 20% CaO target on 4 different substrates. Vertical dash lines are drawn to mark peak positions for comparison. c) HAADF STEM image of film deposited from a 10% CaO target showing the co-existence of Ca:TiO₂-B and anatase. A Ca:TiO₂-B grain in a different orientation is encompassed by the dashed line. d) HAADF image of a film deposited from a 20% CaO target. Arrows mark the spots where the Ti-Ca layer is discontinued, as illustrated in the ball model above where the missing part is shaded, representing the atom arrangement in the red box.

direction of the SrTiO₃. The film is mainly comprised of the Ca:TiO₂-B phase in its signature layered bronze structure, with the Ti-Ca interleaved layer turning the regular TiO₂-B structure into a twinned zigzag pattern (refer to the attached crystallographic information file: CaTi5O11.cif). Since the cubic substrate has four equivalent directions on the surface, Ca:TiO₂-B grains can form in four different orientations with its [100] direction aligned along one of the <100> directions on the (001) SrTiO₃ substrate surface. As seen in Figure 1c, the [010] direction of the large Ca:TiO₂-B grain on the top-left side is parallel to the [010] direction of the SrTiO₃ substrate, while the small grain outlined in the top-right corner is viewed along the [100] direction. Such epitaxial relationships at the film-substrate interface are calculated and relaxed by first-principles optimization, as depicted in Figure 2. Such an inherent effect of the crystal symmetry essentially limits the grain size of Ca:TiO₂-B. A few anatase grains growing along its *c*-axis were also observed (Figure 1c). Images taken at lower magnifications indicate that the anatase phase occupies approximately 5-10% of the volume of the film, though it should be noted that most anatase grains are located near the interface with the substrate. Once the Ca:TiO₂-B phase is formed, it offers a good template for continuous upward stacking of atom layers in the *a*-*b* planes, and therefore the film surface is cleanly Ca:TiO₂-B. As the Ca content is increased in the target, the anatase 004 peak is gradually suppressed relative to the Ca:TiO₂-B peaks. The target containing 20% CaO resulted in the best films so far with strongest 001 reflections from the bronze planes (bottom pattern in Figure 1a), and only a trace amount of anatase.

Ca is of vital importance in stabilizing the structure. Figure 1d shows the HAADF image of a film deposited using the 20% CaO target. While the film is comprised entirely of the Ca:TiO₂-B phase,

crystal defects can be identified stemming from where the Ti-Ca interleaved layers are partially missing, creating a somewhat disordered boundary separating two grains, which is possibly caused by slight perturbation of material flow in the PLD plasma plume, or inhomogeneity in the target composition. The fact that the 20% CaO target worked better than the stoichiometric 16.7% CaO target indicates that, in this specific thermodynamic environment during growth, Ti in the targets has a higher efficiency of transferring into the film than Ca does. Such observation helps explain the lower Ca:TiO₂-B purity in films grown from targets that have less Ca content, where the deficiency of Ca starves a few grains into forming TiO₂-anatase.

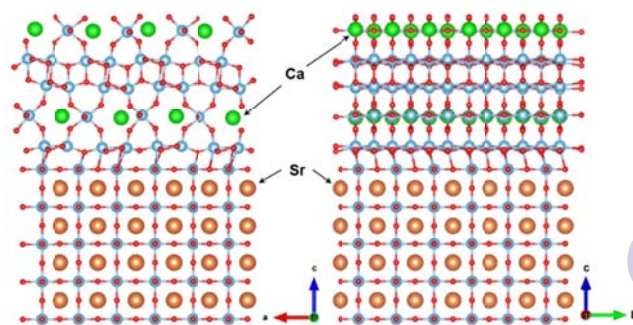


Figure 2. Crystal structure projected along [010] (left) and [100] (right) directions, showing the interfacial atomic structure and epitaxial relationship between Ca:TiO₂-B (001) and SrTiO₃ (001) planes.

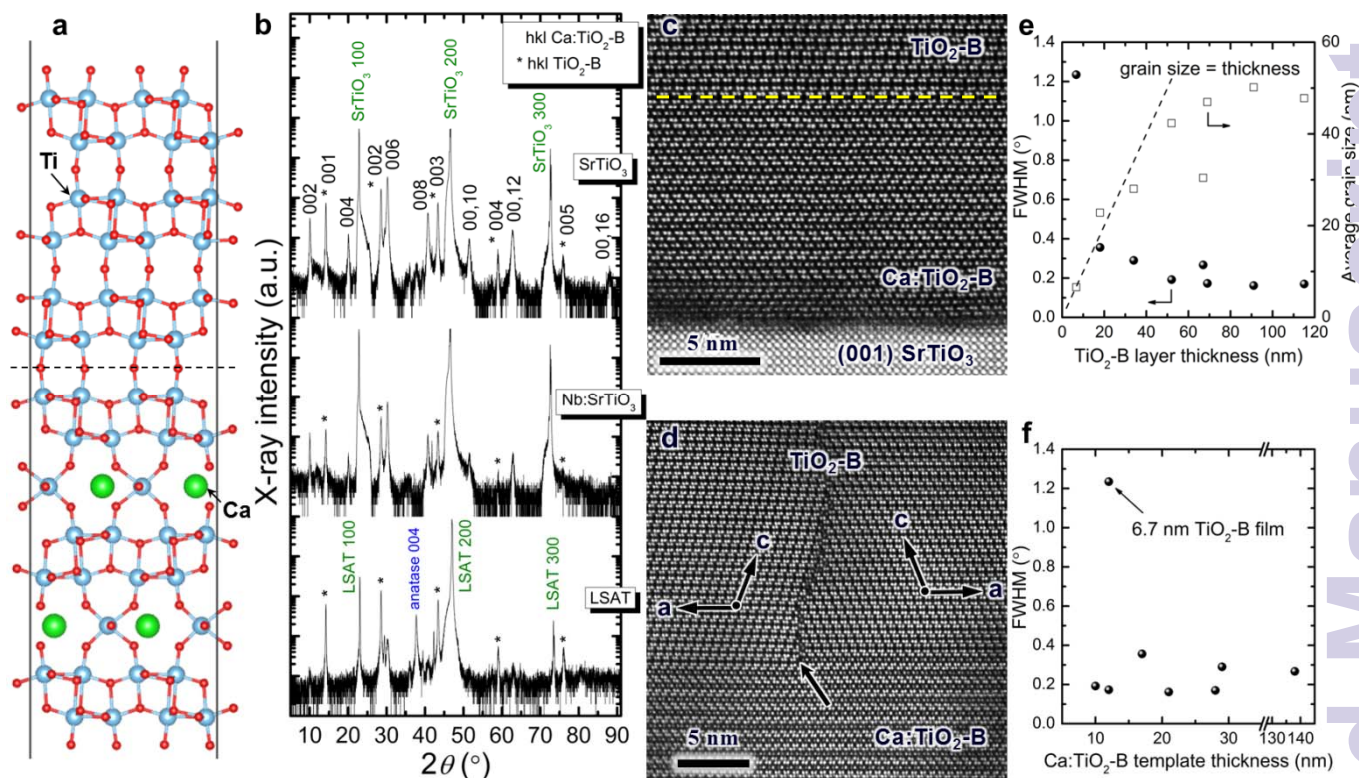


Figure 3. (001) $\text{TiO}_2\text{-B}$ grown on a (001) $\text{Ca:TiO}_2\text{-B}$ template. a) The atomic model projected along $\text{Ca:TiO}_2\text{-B}$'s b -axis showing the epitaxial relationship between the two phases. b) XRD patterns of the dual layer films grown on various (001) substrates. The $\text{Ca:TiO}_2\text{-B}$ template was deposited from a 20% CaO target. c-d) HAADF STEM images of a dual layer film grown on a SrTiO_3 (001) substrate. Dash lines in a) and c) indicate the interface. e) FWHM of the $\text{TiO}_2\text{-B}$ 002 peak as a function of the layer thickness (solid dots), and the average grain size calculated from the FWHM using Scherrer equation (open squares). The dashed line indicates the situation when grain size equals film thickness. f) $\text{TiO}_2\text{-B}$ 002 FWHM as a function of the $\text{Ca:TiO}_2\text{-B}$ template thickness.

To explore the possibility of growing bronze films on other substrates, a few commonly used crystals have been tested, and their lattice structures are listed in Table S1 (ESI[†]).¹⁸ The θ - 2θ XRD patterns of the films deposited on various substrates from a 20% CaO target with growth conditions fixed as above are compared in Figure 1b. Among the five, only LaAlO_3 led to the formation of the $\text{Ca:TiO}_2\text{-B}$ phase, where anatase is also prominent, and no $\text{Ca:TiO}_2\text{-B}$ formation can be identified on the rest. CaTiO_3 phase was found on MgO , while TiO_2 -rutile could be identified on YSZ and Al_2O_3 .^{18,19} The resultant phases were mostly driven by their epitaxial relationship with the substrates. Table S2 (ESI[†]) summarizes the in-plane mismatch at the film-substrate interface, where it is clear that the structure which the films eventually crystallized in is determined by a combination of small lattice mismatch, similar crystal symmetry and target composition.^{20,21} There are a few unidentified peaks, sometimes quite broad, in each XRD pattern, which are likely associated with more complicated phases such as Ti_4O_7 (01-077-1392) or CaTi_2O_4 (04-010-1325) in less crystalline form, although these non-dominant phases were not observed in TEM (typical specimens allow viewing for $\sim 1 \mu\text{m}$ along the interface).

Understanding that (001) SrTiO_3 is by far the most suitable substrate for the growth of $\text{Ca:TiO}_2\text{-B}$, the effects of varying growth temperature, laser energy and O_2 partial pressure were further investigated. In order to monitor the purity of the desired $\text{Ca:TiO}_2\text{-B}$ phase relative to the major impurity, anatase, in this study, a target containing 10% CaO was used so that the anatase 004 peak was usually manifest, as discussed above. Figure S1a (ESI[†]) compares the XRD patterns of the films grown in the temperature range of 600-900 °C with other conditions fixed. The existence of anatase

was observed in all samples, and its 004 peak was strongest at 700 °C. At that same temperature, the $\text{Ca:TiO}_2\text{-B}$ phase started to form showing a broad 006 peak, which became stronger and sharper with increasing temperature until the optimal result at 800 °C, and then broadened and weakened again up to 900 °C. On the other hand, the formation of the $\text{Ca:TiO}_2\text{-B}$ phase was not very sensitive to the laser pulse energy, as samples of similar quality were obtained using laser energy around 200 mJ. However, if the laser pulses were overly powerful, the excess amount of Ti in the plasma plume would force part of the film to crystallize in cubic TiO phase rather than TiO_2 , as seen in Figure S1b (ESI[†]). The impact of O_2 partial pressure on the thin film growth is shown in Figure S1c (ESI[†]). With no O_2 backfilling, anatase formation was prohibited and a faint $\text{Ca:TiO}_2\text{-B}$ 006 peak was observed. The increasing pressure of O_2 helped fill oxygen vacancies in the bronze structure, yielding the best result at 0.05 Torr, beyond which the material flow was scattered and ion path shortened with almost no film deposited at 0.1 Torr.

$\text{Ca:TiO}_2\text{-B}$ can serve as a template for growing regular $\text{TiO}_2\text{-B}$ on top due to the near-perfect lattice match between the two, where their mismatch in the a - b plane is -0.075% (ESI[†], Table S2).²² The crystal structure of $\text{TiO}_2\text{-B}$ epitaxy on $\text{Ca:TiO}_2\text{-B}$ that has been optimized by VASP software²³ is shown in Figure 3a. As a result high quality (001) $\text{TiO}_2\text{-B}$ thin films could be deposited on a (001) $\text{Ca:TiO}_2\text{-B}$ template layer using a pure TiO_2 target under the same growth conditions as for $\text{Ca:TiO}_2\text{-B}$, in contrast to the anatase film obtained from direct deposition of pure TiO_2 on a (001) SrTiO_3 substrate.²⁴ The XRD pattern and a HAADF image of a $\text{TiO}_2\text{-B}/\text{Ca:TiO}_2\text{-B}/\text{SrTiO}_3$ heterostructure are illustrated in Figure 3b (top part) and 3c, corresponding well with the atomic model. The

templating effect in such a dual layer film is obvious. Depending on the terminating surface in its zigzag structure of the Ca:TiO₂-B layer, the TiO₂-B phase could be growing along two opposite directions in the upward stacking of atom layers in the *a-b* planes, as seen in Figure 3d. Originating from the defect (indicated by the arrow) of a partially missing Ti-Ca interleaved layer, the Ca:TiO₂-B phase terminates with different surfaces that are two Ti layers apart, resulting in an anti-phase boundary above it where two TiO₂-B grains collide.

Crystal quality of the TiO₂-B thin films was then examined by monitoring the full width at half maximum (FWHM) of the TiO₂-B 002 (strongest) XRD peak. Both the FWHM values, as well as the average grain sizes calculated using the Scherrer equation, are plotted as functions of the TiO₂-B film thickness in Figure 3e. Below ~40 nm, the grain size increases proportionally with the film thickness, resulting in a decreasing FWHM. As the thickness further increases, the grain size is often limited in the lateral dimension by crystal defects such as the anti-phase boundary in Figure 3d, and shows a saturation behavior at ~50 nm, corresponding to a FWHM of ~0.162°. The dependence of TiO₂-B 002 FWHM on the thickness of the underlying Ca:TiO₂-B template layer, however, is not significant. Except for the relatively large value associated with the smallest TiO₂-B thickness, the FWHM is almost independent on the template thickness over a wide range, from 10 to 140 nm, as seen in Figure 3f.

These results suggest that the templating effect can be transferred to other systems for TiO₂-B applications, as long as a well-defined Ca:TiO₂-B (001) surface is formed. For instance, a conductive substrate is convenient for current collection when investigating the electrochemical properties of TiO₂-B as a thin film anode in lithium-ion batteries.¹⁶ Using a 0.15 at.% Nb doped SrTiO₃ (001) substrate (resistivity ~0.08 Ω cm), a high quality dual layer film was also achieved (Figure 3b). Similar results were acquired from another sample grown on (001) LSAT, where it was demonstrated that the thicknesses of the two phases can be adjusted by controlling respective growth times: deposition time for TiO₂-B was doubled (2 hr to 4 hr) while it was decreased to 1/6 for Ca:TiO₂-B (2 hr to 20 min), producing relatively stronger TiO₂-B peaks in XRD (Figure 3b). A substantial amount of anatase existed in the Ca:TiO₂-B films grown on LSAT, likely caused by the fact that anatase has a smaller in-plane mismatch with LSAT than with SrTiO₃ (ESI[†], Table S2). Similarly, since Ca:TiO₂-B proves to have a good epitaxy on (001) SrTiO₃, the TiO₂-B/Ca:TiO₂-B dual layer structure may be grown on many other substrates where a (001) SrTiO₃ buffer layer can be fabricated. Owing to the layer-by-layer growth mechanism of these structures, the Ca:TiO₂-B film usually has a rather smooth surface with a 1.77 nm root-mean-square (rms) roughness, which translates well to the TiO₂-B layer above it, as shown by the atomic force microscopy (AFM) images in Figure S2a and S2b (ESI[†]), where the hills and valleys in the morphology are possibly associated with crystal defects that extend to the surface (e.g. Figure 1d).

In summary, high quality TiO₂-B and Ca:TiO₂-B thin films with well-controlled lattice orientation and smooth surface can be fabricated on various substrates through a completely waterless process. Building on guidelines established here, multilayer devices that utilize both the bulk and the surface of these attractive materials may prove promising in a wider range of applications.

This work was supported by Ford Motor Company under a University Research Proposal grant, the National Science Foundation through Grants CBET-1159240 and DMR-0723032 (aberration-corrected TEM), partially by the U.S. Department of Energy, Office of Basic Energy Sciences, Division of Materials Sciences and Engineering under Awards DE-FG02-07ER46416

(TEM experiments), and the Natural Science Foundation of China under Grant 51472254.

Notes and references

- ^a Department of Materials Science and Engineering, University of Michigan, 2300 Hayward St., Ann Arbor, Michigan 48109, USA.
- ^b Department of Chemical Engineering and Materials Science, University of California – Irvine, 816 Engineering Tower, Irvine, California 92697, USA. E-mail: xiaoqing.pan@uci.edu
- [†] Electronic Supplementary Information (ESI) available: structural details, lattice mismatch and surface characterization. See DOI: 10.1039/c000000x/
- 1 R. Marchand, L. Brohan and M. Tournoux, *Mater. Res. Bull.*, 1980, **15**, 1129-1133.
- 2 A. S. Arico, P. Bruce, B. Scrosati, J. M. Tarascon and W. Van Schalkwijk, *Nat. Mater.*, 2005, **4**, 366-377.
- 3 T. Kogure, T. Umezawa, Y. Kotani, A. Matsuda, M. Tatsumisago and T. Minami, *Journal of the American Ceramic Society*, 1999, **82**, 3248-3250.
- 4 A. R. Armstrong, G. Armstrong, J. Canales and P. G. Bruce, *Angewandte Chemie International Edition*, 2004, **43**, 2286-2288.
- 5 G. Armstrong, A. R. Armstrong, J. Canales and P. G. Bruce, *Chemical Communications*, 2005, 2454-2456.
- 6 T. Beuvier, M. Richard-Plouet, M. Mancini-Le Granvalet, T. Brousse, O. Crosnier and L. Brohan, *Inorganic Chemistry*, 2010, **49**, 8457-8464.
- 7 H. Liu, Z. Bi, X.-G. Sun, R. R. Unocic, M. P. Paranthaman, S. Dai and C. M. Brown, *Advanced Materials*, 2011, **23**, 3450-3454.
- 8 S. Liu, H. Jia, L. Han, J. Wang, P. Gao, D. Xu, J. Yang and S. Cheng, *Advanced Materials*, 2012, **24**, 3201-3204.
- 9 W. J. Zhou, L. G. Gai, P. G. Hu, J. J. Cui, X. Y. Liu, D. Z. Wang, G. H. Li, H. D. Jiang, D. Liu, H. Liu and J. Y. Wang, *Crystengcomm*, 2011, **11**, 6643-6649.
- 10 S. H. Liu, Z. Y. Wang, C. Yu, H. B. Wu, G. Wang, Q. Dong, J. S. Qiu, J. Eychmuller and X. W. Lou, *Advanced Materials*, 2013, **25**, 3462-3467.
- 11 D. J. Yang, H. W. Liu, Z. F. Zheng, Y. Yuan, J. C. Zhao, E. R. Waclawik, X. B. Ke and H. Y. Zhu, *J. Am. Chem. Soc.*, 2009, **131**, 17885-17893.
- 12 Y. G. Andreev, P. M. Panchmatia, Z. Liu, S. C. Parker, M. S. Islam and P. G. Bruce, *J. Am. Chem. Soc.*, 2014, **136**, 6306-6312.
- 13 V. Etacheri, Y. Kuo, A. Van der Ven and B. M. Bartlett, *Journal of Materials Chemistry A*, 2013, **1**, 12028-12032.
- 14 A. G. Dylla, G. Henkelman and K. J. Stevenson, *Accounts of Chemical Research*, 2013, **46**, 1104-1112.
- 15 J. Fang, F. Wang, K. Qian, H. Z. Bao, Z. Q. Jiang and W. X. Huang, *J. Phys. Chem. C*, 2008, **112**, 18150-18156.
- 16 K. Zhang, M. B. Katz, B. H. Li, S. J. Kim, X. F. Du, X. G. Hao, J. P. Jokisaari, S. Y. Zhang, G. W. Graham, A. Van der Ven, B. M. Bartlett and X. Q. Pan, *Advanced Materials*, 2014, **26**, 7365-7370.
- 17 N. Erdman, K. R. Poepplmeier, M. Asta, O. Warschkow, D. E. Ellis and L. D. Marks, *Nature*, 2002, **419**, 55-58.
- 18 A. Lotnyk, S. Senz and D. Hesse, *Thin Solid Films*, 2007, **515**, 3439-3447.
- 19 R. Shinohara, T. Yamaki, S. Yamamoto, H. Itoh and K. Asai, *Journal of Materials Science Letters*, 2002, **21**, 967-969.
- 20 C. F. Guo, J. M. Zhang, M. Wang, Y. Tian and Q. Liu, *Small*, 2013, **9**, 2394-2398.
- 21 C. F. Guo, S. H. Cao, J. M. Zhang, H. Y. Tang, S. M. Guo, Y. Tian and Q. Liu, *J. Am. Chem. Soc.*, 2011, **133**, 8211-8215.
- 22 T. P. Feist and P. K. Davies, *J. Solid State Chem.*, 1992, **101**, 275-295.
- 23 G. Kresse and J. Hafner, *Phys. Rev. B*, 1993, **48**, 13115-13118.
- 24 S. Yamamoto, T. Sumita, T. Yamaki, A. Miyashita and H. Naramoto, *J. Cryst. Growth*, 2002, **237**, 569-573.